Competing adsorption of H and CO on Pd-alloy surfaces: Mechanistic insight into the mitigating effect of Cu on CO poisoning

Acta Materialia 316 (2026) 122507

Contents lists available at ScienceDirect

Acta Materialia

journal homepage: www.elsevier.com/locate/actamat

Full length article

Competing adsorption of H and CO on Pd-alloy surfaces: Mechanistic insight into the mitigating effect of Cu on CO poisoning

Pernilla Ekborg-Tanner, Paul Erhart *

Department of Physics and Astronomy, Chalmers University of Technology, SE 412 96 Gothenburg, Sweden

ARTICLE INFO

Keywords:
Alloy surfaces
Surface phase diagrams
Coadsorption
Hydrogen sensing
Multiscale modeling

ABSTRACT

Multi-component alloys offer broad tunability for materials science applications, but are highly sensitive to operating conditions through adsorption and segregation phenomena. Here, we study Pd–Au–Cu alloy surfaces in H_2 and CO environments motivated by their use in H technologies, where alloying can mitigate limitations intrinsic to Pd such as CO poisoning. To this end, we establish a framework combining machine-learned interatomic potentials trained on density-functional theory data with cluster expansions, with effectively no limitations on training set size.

By constructing continuous surface phase diagrams for H–CO coadsorption, we find that adsorption under operating conditions is governed by the H coverage during the preceding annealing. Au-rich surfaces, formed under H-poor conditions, suppress both CO and H adsorption, while H-rich conditions yield Pd-rich surfaces that promote CO and H adsorption. Furthermore, Pd-rich alloy surfaces maintain higher H coverages compared to pure Pd at relevant CO partial pressures, indicating improved CO poisoning resistance. The coadsorption behavior of PdAuCu alloys is indistinguishable from that of PdAu alloys, despite experimental observations of Cu, specifically, mitigating CO poisoning. However, kinetic barriers of H sorption in dilute alloys indicate that H pathways near Au are highly unfavorable, while Cu leaves the energetics unchanged compared to pure Pd. Based on these findings and the experimental evidence, we hypothesize that alloying promotes H adsorption while Cu, specifically, preserves viable H absorption pathways in the presence of CO.

1. Introduction

Multi-component materials underpin applications ranging from chemical sensing and catalysis to energy conversion and structural engineering. Under realistic operating conditions, such as finite temperatures and reactive gas environments, the surface properties of these materials are often changed due to adsorption and segregation [1,2]. Such processes critically influence materials performance by altering kinetic, thermodynamic, electronic, optical, and mechanical properties. Understanding and controlling these phenomena is, therefore, essential for the design of functional multi-component materials. Yet, current modeling approaches still struggle to capture the immense combinatorial and structural complexity of these systems, particularly when adsorbates, surfaces, and thermodynamic effects all come into play.

Pd-based nanoalloys have received considerable attention, especially in the context of optical hydrogen sensing, which exploits changes in the position and shape of the localized surface plasmon resonance (LSPR) of Pd nanoparticles upon hydrogen sorption [3]. While the basic working principle is well established, further improvements are needed to make this technology robust under realistic conditions. Pure Pd sensors suffer from hysteresis between hydrogen absorption and desorption, as well as carbon monoxide (CO) poisoning caused by the preferential adsorption of CO over H [4]. These effects directly compromise the reliability and stability of LSPR-based hydrogen sensors. Alloying is an effective mitigation strategy, as the addition of approximately 25 % Au suppresses hysteresis, while introducing only 5 % Cu has been found to reduce CO poisoning [5–7]. While the effect of Au on hysteresis is well understood [8], the mechanism behind the mitigating effect of Cu is not yet understood, especially since Cu rarely resides directly at the surface [2].

Introducing multiple alloying elements and adsorbate species, however, substantially enlarges the design space and creates additional complexity due to the nontrivial coupling between adsorption and segregation. Prior work has addressed components of this challenge. Adsorption and coadsorption on pure metal surfaces have been treated with lattice-gas CEs [9–11]. Surface segregation in alloys has likewise been studied extensively, both in vacuum [12,13] and in the presence of a single adsorbate species [14], where direct DFT calculations [15–17] and CE-based MC treatments [2,18] have shown that

* Corresponding author.
E-mail address: erhart@chalmers.se (P. Erhart).

https://doi.org/10.1016/j.actamat.2026.122507
Received 27 February 2026; Received in revised form 5 June 2026; Accepted 27 June 2026
Available online 2 July 2026

adsorption can dramatically change the surface composition. Related studies on alloy nanoparticles couple segregation and adsorption on a shared metal/adsorbate/vacancy lattice [19,20]. Recent methodological advances have extended these capabilities to increasingly complex systems, either by augmenting CEs with machine learning [21,22] or by replacing CEs with MLIPs [23–27]. To our knowledge, however, no prior study of multi-component materials under reactive conditions has simultaneously addressed ternary alloy segregation, multi-species adsorption and multiple surface facets.

To comprehensively model such a system, a framework is required that (i) captures subtle energy differences between competing atomic arrangements in the bulk and at surfaces, (ii) treats the interactions among adsorbates and between adsorbates and surfaces with sufficient accuracy, and (iii) enables efficient sampling across a range of thermodynamic boundary conditions, including temperature and gas pressure. Here, we address these challenges by combining MLIPs trained on DFT calculations with CEs and MC sampling, and apply this approach to study the competing adsorption of H and CO on pristine {111}, {110}, and {100} surfaces of PdAuCu alloys. The focus is on the initial surface adsorption step, and H absorption into the bulk is not considered.

We find that the surface chemistry of PdAuCu alloys under H–CO coadsorption is governed primarily by the H coverage during annealing rather than the alloy composition. In the coadsorption limit, alloying generally improves CO poisoning resistance, but this improvement is insensitive to alloy composition, ruling out adsorption thermodynamics as the origin of the experimentally observed Cu-specific benefit. However, kinetic barriers for H sorption in the dilute alloy limit show that while absorption paths via Au atoms are highly unfavorable, paths via Cu or Pd are energetically similar, suggesting that the benefit of Cu might be related to the sorption kinetics.

2. Methodology

Electronic-structure calculations, most commonly based on DFT, remain the common standard for accuracy when modeling extended systems. However, their high computational cost renders them impractical for systems with multiple alloying components, low symmetries, and finite-temperature effects such as mixing, ordering, and segregation.

CEs provide an efficient and well-established framework for modeling configurational complexity in alloys [28]. They have been successfully applied to multi-component bulk alloys [29] as well as surfaces with adsorbates [2,12,30]. In low-symmetry systems, such as surfaces, the number of interaction parameters grows rapidly, raising the demand for training data, which is still most commonly generated using DFT calculations. While Bayesian approaches help manage this growth by incorporating physical insight via priors [30], the combinatorial explosion that occurs when increasing the number of components remains challenging [21,29,31]. When multiple surface orientations are relevant, it is furthermore desirable for the different surface-specific CEs to yield consistent behavior in the bulk limit. Without such consistency, predictions of surface segregation across facets may become unreliable, which poses the additional challenge of reconciling models for different surface orientations.

In the last decade, MLIPs have emerged as powerful tools that bridge the accuracy of electronic-structure methods with the efficiency of empirical potentials. They open the possibility of serving as intermediaries for constructing CEs, offering accuracy at scale [32]. While MLIPs have already been deployed in hybrid molecular dynamics (MD)-MC simulations to model ordering and mixing in bulk alloys [33,34], these approaches are not well suited for sampling adsorbate–gas equilibria. For this purpose, lattice-based CE-MC simulations remain the most effective strategy.

To tackle the above challenges, we adopt the following approach. To cut the cost of DFT calculations, we build MLIPs based on both the NEP and the MACE architecture. Specifically, we use NEP models, which are up to three orders of magnitude faster than MACE (Fig. S3),

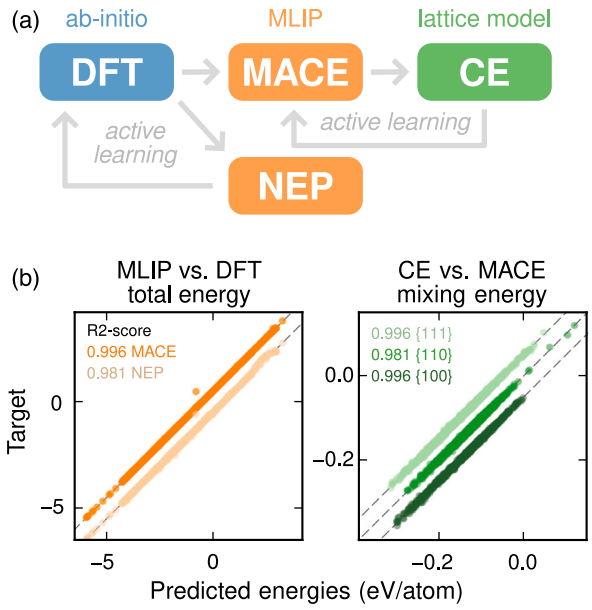

Fig. 1. Model development. (a) Schematic illustration of the computational framework. (b) Model errors for the MLIPs and the CE. Note that the data has been systematically shifted along the y-axis to allow for clearer visualization of the different models.

to build a comprehensive set of reference data via active learning, and MACE models, which yield higher accuracy, to generate reference data for training CE models. The CEs are constructed for {111}, {110}, and {100} surfaces that are coupled to the same underlying bulk model through constraints, and include Au, Pd, and Cu on the metal lattice as well as H and CO on the adsorbate lattices. Training data for these models are generated from structural relaxation using the MACE model, such that relaxation effects are implicitly included, in an active learning loop. In taking this approach, we exploit that different types of predictions require different levels of accuracy.

2.1. Machine-learned interatomic potentials

We construct MLIPs using the fourth-generation NEP framework [34,35], the separable neuroevolution strategy [36] and the iterative procedure described in Ref. [37], utilizing the GPUMD [35,38] and CALORINE [39] packages, as detailed in Supp. Note 1. A combination of structure enumeration [40,41], nudged elastic band (NEB) [42–44] pathways and MD trajectories are used to generate bulk and surface structures in an active training loop, using the NEP models and the ASE [45], HIPHIVE [46], and ICET packages [47,48] (Supp. Note 3). The final set of reference structures comprises 18 403 structures, corresponding to a total of 586 006 atoms (see Table S3 for an overview). Using the final set of reference structures, we construct a MACE model [49] using the MACE-TORCH package [50] as described in Supp. Note 2.

2.2. Density functional theory calculations

The MLIPs are fitted using forces, energies, and virials obtained from DFT calculations, employing the van-der-Waals density functional with the consistent exchange (vdW-DF-cx) method [51,52] as implemented in the Vienna ab-initio simulation package [53,54] using projector-augmented wave setups [55,56] with a plane wave energy cutoff of 520 eV. The Brillouin zone is sampled with automatically generated **k**-point grids with a maximum spacing of 0.1/Å.

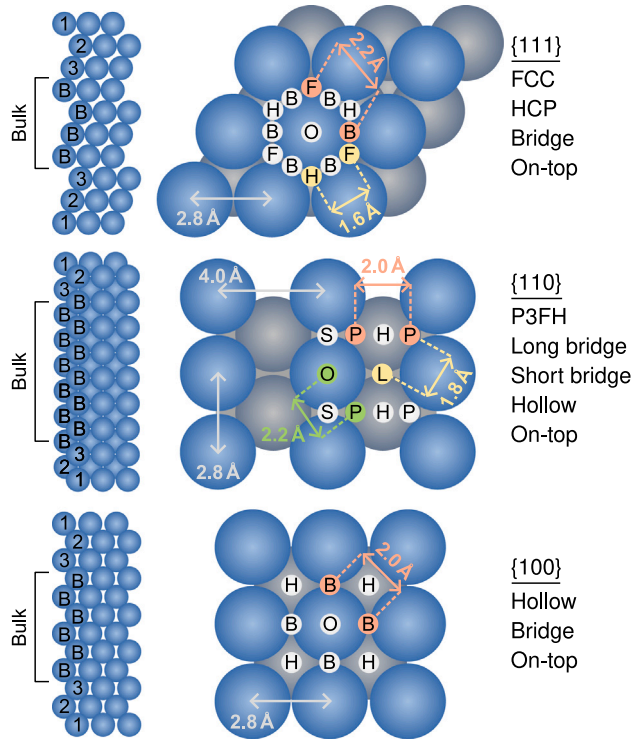

Fig. 2. Schematic illustration of the surface slabs and their respective adsorption sites. Side views of the surface slabs (to the left) with the surface layers and bulk region indicated. Top views of the surfaces (to the right) with blue atoms for the top layer, gray atoms for the subsequent layers. The smaller atoms show the adsorption sites labeled by their first letter. The arrows between sites indicate their three-dimensional assuming a 4.0 Å lattice parameter. (For interpretation of the references to color in this figure legend, the reader is referred to the web version of this article.)

2.3. Cluster expansion construction

CEs are constructed to model the adsorption of H and CO on pristine face-centered cubic (FCC) alloy surface slabs with {111}, {110} and {100} orientation, using the ICET package [47] following the procedure outlined in Ref. [48]. The CEs predict the mixing energy based on training data obtained by atomic relaxation and energy calculation using the MACE model. The mixing energies are calculated by using the energy per atom of a pure metal slab for the metal species and the molecular ground state energy (divided by 2 for H_2) for the adsorbate species. Fig. 2 shows all atomic sites of the slab and adsorbates. The number of layers varies between the slabs to achieve a similar slab thickness, with 10 layers for {111}, 18 for {110} and 12 for {100}.

The adsorbate sublattice represents an open system and can be occupied by H, CO, or vacancies. All relevant adsorption sites are considered, which allows for configurations with coverages far beyond the relevant limit. Since we do not take into account H sorption into the bulk, only surface coverages up to the limit where entering the subsurface becomes favorable are of interest. This corresponds to a 1:1 ratio between adsorbate and surface metal atoms for {111} and {100} and 2:1 for {110} (Fig. S6). The larger allowed coverage on {110} surfaces is a consequence of the large surface area of {110} where almost the entire second atomic layer is exposed (Fig. 2). For this reason, we define 100 % surface coverage on {110} to mean a 2:1 ratio, as opposed to 1:1 for the other facets, which allows for a fairer comparison between the surface orientations.

Cutoffs are selected to include pairs and triplets up to distances of 8.0 Å and 5.0 Å, respectively, for a 4.0 Å lattice parameter. The number of interaction parameters depends on the number of layers and adsorption sites and ranges from 3300 ({100}) to 9600 ({110}) for the systems considered here. In the context of CE models, these are very large parameter spaces which would be difficult to fit properly using conventional approaches. To overcome this challenge, we exploit pruning and merging of clusters.

Because the adsorbate lattice contains many close-lying, symmetrically inequivalent sites, their interactions will contribute to a very large number of inequivalent clusters. Many of these correspond to interaction lengths shorter than the minimal distance between adsorbates at the maximum coverage limit. For this reason, we introduce a lower cutoff radius of 1.5 Å for {111} and {100}, and 1.2 Å for {110} and prune all clusters below this limit. We also make the pragmatic choice of pruning all adsorbate–adsorbate interactions longer than the FCC nearest-neighbor distance (2.8 Å) as well as all adsorbate-slab interactions extending below the third layer. We note that as a result, the coverage dependence of the adsorption energies is not fully reproduced by the CEs (Fig. S5), but the residual coverage dependence has a magnitude comparable to the overall adsorption energy error (Fig. 3b).

Merging, in this context, refers to grouping together clusters that are not strictly symmetrically equivalent but can be assumed to be similar [2,48]. This includes clusters far from the surface region, which should be similar to the equivalent cluster of a bulk system. Here, we consider the three outermost atomic layers to be the surface region and all inner layers to be the bulk, and merge all clusters with the same radius that consist of bulk sites only, as described in Ref. [48]. To ensure the CE models for the different surface orientations yield a correct and consistent description of the bulk region, we first construct a bulk CE for the PdAuCu system based on approximately 900 enumerated structures with up to 9 atoms in the unit cell and up to 50 % Au and 20 % Cu. The resulting bulk interaction parameters are used in place of the merged bulk interactions for the surface slabs.

Pruning, merging and fixing the bulk interactions cuts the number of orbits by half, resulting in 2000 to 4500 parameters, which can be further reduced by regularization. Because these numbers are still too large to efficiently apply common advanced linear regression methods, a two step approach is adapted. First, an initial feature selection is performed using the least absolute shrinkage and selection operator (LASSO) [57] resulting in 1000 to 1400 parameters. Second, automatic relevance detection regression (ARDR) [58] is used to fit the final model after tuning the hyperparameters to achieve the lowest number of features with a converged R2-score (Fig. S7). We use LASSO and ARDR as implemented in SCIKIT-LEARN [59] via the TRAINSTATION package [60].

Atomic structures for the training set are generated and selected using an active learning approach and relaxed using the MACE model, keeping the in-plane lattice parameter fixed based on interpolation of lattice parameters from relaxed bulk structures. An initial dataset, consisting of 300 structures with approximately orthogonal cluster vectors (following the method outlined in Ref. [48]), is used to train an ensemble of CEs. A CE corresponding to the mean of the ensemble is used to run 300 short annealing MC simulations. The ensemble of CEs is used to calculate the uncertainty in energy across these trajectories, and the structure with the highest uncertainty for each trajectory is added to the training set. This process is repeated four times, at which point the root mean square error (RMSE) is no longer improving (Fig. S7).

For the final models, we also include the structures generated specifically for calculating the adsorption and segregation energies as well as similar sets of structures generated for adsorbate-free CEs in parallel, resulting in about 2800 structures for each orientation. The final models show excellent agreement with the MACE training data (Fig. 1b). For the {111} surface, the final model has 323 features (i.e., non-zero parameters) and achieves a validation RMSE of 3.8 meV/metal atom, for the {110} surface the final model has 281 features and achieves a validation RMSE of 6.4 meV/metal atom, and finally, for the {100} surface the final mode has 195 features and yields a validation RMSE

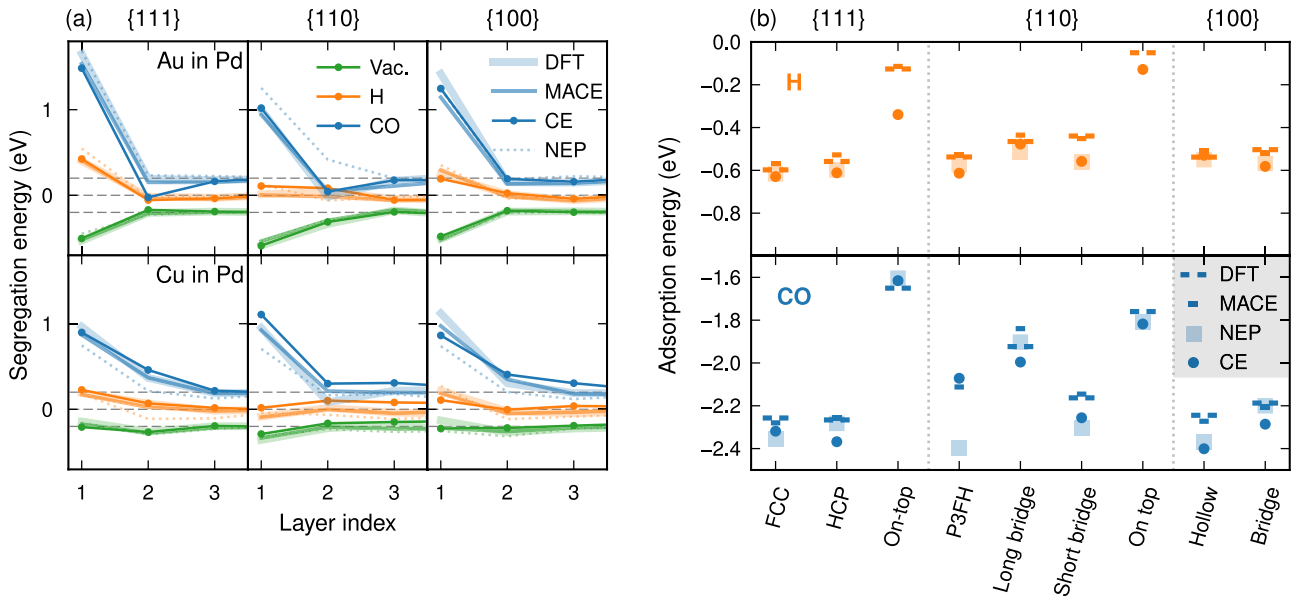

Fig. 3. Model performance for surface properties. (a) Segregation energies from DFT, NEP, MACE, and CE for dilute Pd alloys in vacuum, H_2 and CO (100 % coverage). Negative (positive) values indicate that the minority species prefers (avoids) residing in the surface region. Note that the curves are shifted along the y-axis for better visualization. (b) Adsorption energies for H and CO on Pd (25 % coverage) for all models. Additional sites and adsorption energies on Cu and Au can be found in Fig. S4.

of 3.7 meV/metal atom. The models are further validated by comparing the predicted segregation and adsorption energies with DFT and MLIP data (Fig. 3), which demonstrates excellent agreement. Here, the segregation energy is calculated for a single Au (Cu) atom in different layers of a 2×2 Pd slab, compared to the energy of placing the minority atom in the bulk.

2.4. Monte Carlo simulations

To study the surface-adsorbate system under various conditions, MC simulations are performed using the MCHAMMER package [47]. The structures studied typically consist of $6 \times 6 \times n_{\text{layers}}$ metal atoms and up to 1 (for {111} and {100}) or 2 (for {110}) monolayers of H or CO and the simulation runs for 100 MC cycles.

MC simulations of an adsorbate lattice need to account for the fact that many unfavorable configurations will not be represented well by the CE, since the adsorbates can move to more favorable configurations during relaxation. Especially when using the full adsorbate lattice (i.e., all adsorption sites), distances between neighboring sites are typically too short to allow for occupation of both sites in atomic relaxation as well as in reality. To account for this, we impose a minimal distance between occupied adsorbate sites (1.9 Å for {111} and {110}, 2.1 Å for {100} Fig. 2), which still allows for reaching the maximum coverage before absorption to the subsurface becomes favorable (Fig. S6). In addition, some adsorbate sites are not well represented in the training set since structural relaxation moves the adsorbates to a more favorable neighboring site, and are therefore not captured by the CEs (bridge for {111}, hollow for {110} and on-top for {100}, see Fig. S4). These sites are therefore excluded in the MC simulations.

The MC simulations are performed in multiple steps to mimic the experimentally studied systems, which were annealed in a H_2 environment (corresponding to 40 mbar H partial pressure) at 773 K before the optical measurements were performed in ambient conditions and varying H_2 and CO partial pressures. First, the slab configuration is obtained from MC simulations at 773 K and a varying H coverage. The simulation uses three separate canonical ensembles for the bulk, surface, and adsorbate subsystems. The total concentration of the surface region is prescribed by interpolating from a set of preceding simulations in which the bulk and surface were equilibrated together as a single subsystem, spanning the full range of H coverages. This procedure allows for control of the bulk composition while equilibrating the surface with both the bulk and the adsorbates. Then, the co-adsorption phenomena during the experimental measurements are simulated via MC simulations at 300 K. Due to the different timescales of adsorption [6,7] and chemical reordering [61,62] of the slab configuration, where the latter is much slower, we keep the slab configuration fixed (from the previous simulation) while the adsorbate sublattices are equilibrated within a semi-grand canonical (SGC) ensemble controlled by the H and CO chemical potentials.

To prevent the adsorbate configuration from freezing in, swaps in the SGC ensemble are mixed with swaps in a canonical ensemble for the adsorbate sublattice, which enables swaps between two sites. This scheme enables moving an adsorbate from, e.g., a bridge site to a neighboring FCC site without having to first switch the site to vacuum which rarely will be an accepted move.

3. Results and discussion

3.1. Surface phase diagram construction

Traditionally, SPDs are constructed by calculating the free energy per primitive cell (or area) as a function of chemical potential at a few selected surface coverages and identifying the minimum energy phase. In Fig. 4, we show this process for the Pd {111} surface. In Fig. 4a, the free energy in the 0 K limit,

$$G(\theta_{\text{H}}, \theta_{\text{CO}} = 0) = E^{\text{mix}}(\theta_{\text{H}}, \theta_{\text{CO}}) - \theta_{\text{H}}\mu_{\text{H}}, \tag{1}$$

is calculated from the CE mixing energy (from which the gas phase H and CO energies in relation to their respective coverages θ have already been subtracted) and the chemical potential. The convex hull indicates the stable adsorbate coverage in a certain chemical potential interval. By repeating this for multiple combinations of H and CO coverages, a two-dimensional SPD can be constructed (Fig. 4b). While this example uses a CE, it is straightforward to construct this kind of surface diagram using DFT calculations for pure metal surfaces and certain high-symmetry alloys (see Supp. Note 4, Fig. S9). For more complex systems, however, the number of configurations to consider quickly

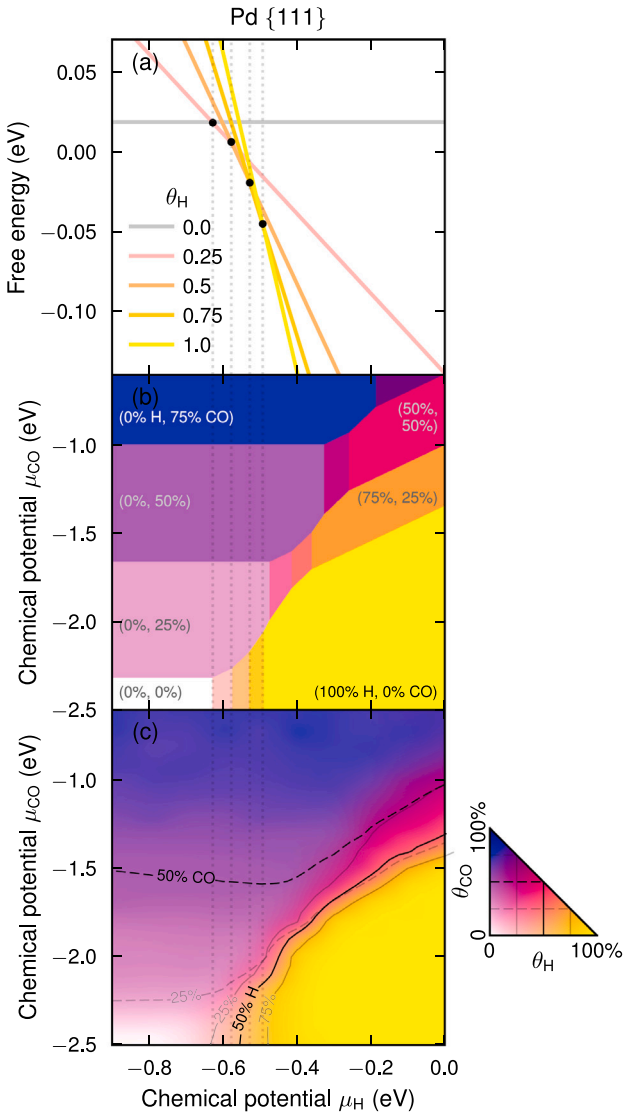

Fig. 4. SPD construction for Pd {111}. Traditionally, SPDs are constructed by calculating the free energy as a function of the chemical potential for specific coverages (a) and translating the convex hull to a discrete surface diagram (b). MC sampling of CEs allows for efficient sampling of surface coverage(s) as a function of chemical potential(s) which results in continuous surface diagrams (c).

becomes unmanageable. In addition, finite temperatures require treatment of the configurational entropy. Using a CE in combination with MC simulations allows for efficient thermodynamic sampling, including configurational entropy contributions, in the SGC ensemble where the chemical potentials are controlled, which results in a continuous SPD (Fig. 4c).

3.2. Pressure conversion

In most cases, the partial pressure p is more relevant than the chemical potential μ. If ideal gas behavior can be assumed, the two are connected via the relations

$$\mu_H(T,p) = \frac{1}{2}\left(\mu^0_{H_2}(T) + kT\ln\frac{p_{H_2}}{p^0}\right) \quad (2)$$

$$\mu_{CO}(T,p) = \mu^0_{CO}(T) + kT\ln\frac{p_{CO}}{p^0} \quad (3)$$

for H and CO, respectively. The reference chemical potential $\mu^0(T)$, defined at a reference partial pressure p^0, can, in principle, be obtained from thermodynamic tables [66]. This approach, however, suffers from the fact that adsorption energies are generally associated with a significant error in DFT calculations, leading to an effective shift of the chemical potential. In the context of our modeling framework, this approach suffers from the fact that the temperature dependence of the adsorbed molecules is limited to configurational entropy, while the full temperature dependence is accounted for with regard to the gas phase.

In some cases, one can find an observable that can be measured experimentally and calculated in the modeling framework and use this as a basis for calculating the reference. In the present work, the adsorbate coverage at a given temperature can be used for this purpose by linking the coverage as a function of chemical potential from MC simulations to experimental observations of coverage as a function of partial pressure. With this approach, the full temperature dependence is implicitly taken into account, but the availability of experimental data at relevant conditions as well as uncertainty in the measurements are potential issues.

In Fig. 5 we show our approach to pressure conversion. The H coverage on pure Pd is obtained as a function of the H chemical potential (Fig. 5a) from MC simulations. Experimental records of H coverage at known H partial pressure and temperature [63–65] (Fig. 5b) are then matched to the MC results and used to calculate μ^0, which can be fitted by a simple temperature-dependent function. In Fig. 5c we show this (linear) fit as well as $\mu^0(T)$ calculated from the NIST-JANAF thermodynamic tables [66] and a fit based on the bulk hydride formation from Ref. [8]. Note that while the latter shows good agreement for well-corroborated experimental data, it does not explicitly account for the difference between modeling surface adsorption and bulk absorption of H. The shaded regions correspond to an offset equal to the RMSE of the linear fit in the 200 K to 500 K interval. The NIST-JANAF data is corrected by a constant shift of −0.2 eV based on the difference between the CE H adsorption energy (−0.63 eV) and experimental reports [4,73], (∼ − 0.43 eV). Except for the low-temperature limit, the experimental data is well represented. It should, however, be noted that most of the experimental data temperatures indicate very low (sub-percent) coverage with H diffusion to the bulk [64]. For this reason, the only data point with substantial coverage at a relevant temperature (highlighted in Fig. 5a–c) was given a larger weight in the fit. (The fitting procedure included additional sources of experimental data for other surface orientations, see Fig. S10.)

In Fig. 5d–f the analysis of the pressure conversion procedure is shown for CO. The MC simulations display a stair-like behavior for the CO coverage, indicating a preference for ordered phases at 33, 50 and 67 % CO coverage (see Fig. S11 for site-specific coverages) and saturation at 75 % in line with experimental observations [69]. CO adsorption on Pd has been well-studied for the past decades and experimental reports of the CO coverage over a wide range of pressures and temperatures are available [67–72]. The calculated values for $\mu^0(T)$ have some spread, but overall seem to follow a linear trend that is captured by the fit. The calculation based on the NIST-JANAF thermodynamic tables [66] include a correction shift of −0.8 eV based on the approximated difference between the CE H adsorption energy (∼ − 2.3 eV) and experimental reports [72,74], (∼ − 1.5 eV). The NIST-JANAF reference differs from the fitted function in slope and offset.

In Fig. 5b, e we show how the pressure conversion changes with the different approaches to calculating μ^0. All three approaches are subject to systematic limitations, and together span a range of up to three orders of magnitude in partial pressure. We emphasize that this observation highlights the inherent difficulty in accurate conversion between chemical potential and partial pressure, rather than a flaw in our methodology. The resulting uncertainty is, however, too large to allow for meaningful quantitative partial pressure conversion, and following results will therefore be presented in chemical potential space with the associated relevant pressure ranges indicated. For CO, we rely

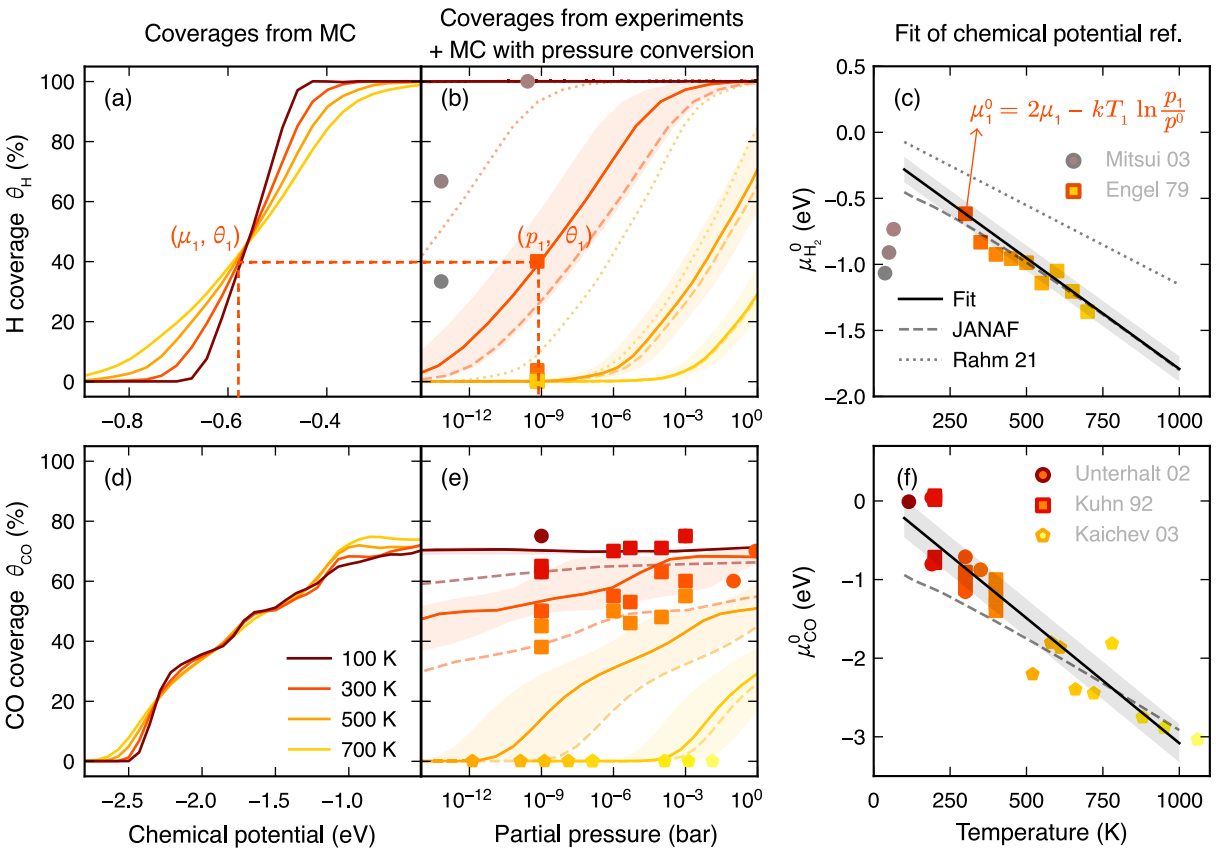

Fig. 5. Conversion between chemical potential and pressure for Pd. (a) H coverage vs. chemical potential obtained from MC simulations. (b) Experimental records of H coverage vs. partial pressure from Mitsui 03 [63], Engel 79 [64], and additional sources (see Fig. S10) [65]. (c) Fit of the reference chemical potential based on the data in (a) and (b) as well as the calculated reference chemical potential based on tabulated thermodynamic data (JANAF [66]) or computational models (Rahm 21 [8]). Once the reference chemical potential is known, the MC data (a) can be converted from chemical potential to partial pressure, as shown in (b) for the different references. (d–f) show the same process for CO with experimental data for Pd:CO from Unterhalt 02 [67], Kuhn 92 [68], Kaichev 03 [69], and additional sources (see Fig. S10) [70–72]. Note that the legends are shared across each row.

on the fit with error bars due to the well-corroborated experimental data and lacking treatment of vibrations in the NIST-JANAF approach. Due to the limited amount of experimental data for H, we use all three approaches to determining μ^0 to span the pressure region. Nevertheless, by combining these pressure ranges with experimental observations, meaningful conclusions about the relevant operating conditions can be drawn.

3.3. Influence of preparation conditions

In the following we present SPDs for Pd-alloy surfaces and study how the preparation conditions affect the H and CO coadsorption. By preparation conditions we refer to the environment in which the slab configuration equilibrates, which in the present work is set up to mimic the experimental procedure of annealing the samples at 773 K in a H_2 environment [6,7]. Due to the large uncertainty associated with the pressure conversion, we consider a range of fixed H coverages during annealing rather than specifying the H_2 partial pressure via the H chemical potential. The resulting compositions of the surface region are presented in Fig. S12 to S14.

We then analyze the coadsorption under operation, i.e. in conditions similar to the experimental measurements [6,7], by constructing SPDs for the H and CO coverage as a function of their respective chemical potentials while keeping the slab configuration fixed. The regions corresponding to ambient (0.6 µbar H_2, 0.1 µbar CO [75]) and operating conditions (1 mbar to 100 mbar H_2 [76,77], 0.1 mbar to 5 mbar CO [6,7]) are indicated, where the width is associated with the uncertainty in partial pressure conversion rather than the considered pressure intervals.

Fig. 6 shows SPDs for Pd, $Pd_{75}Au_{25}$, and $Pd_{75}Cu_{25}$ {111}-surfaces prepared by annealing at 773 K with 0 %, 50 % or 100 % H coverage. For $Pd_{75}Au_{25}$, the surface coverage clearly depends on the preparation conditions. Without adsorbed H during annealing, Au segregates to the surface (Fig. S12). This increases the adsorption energy of both CO and H, leading to low coverages (Fig. 6a) and, in particular, almost no H at the surface under operating conditions which would hinder the H_2 sensing ability. With 50 % H during annealing, the surface composition is similar to the bulk which leads to increased adsorption (Fig. 6b). Lastly, with 100 % H, the outermost surface layer is made up almost entirely of Pd which leads to a further increase of the overall coverages (Fig. 6c) resulting in a similar SPD as to the case of pure Pd (Fig. 6d). There is, however, a notable increase in H coverage in the lower right corner of the operating region, suggesting that $Pd_{75}Au_{25}$ with mostly Pd at the surface is superior to Pd in terms of CO adsorption blocking the surface.

For $Pd_{75}Cu_{25}$, the change in H and CO coverages with preparation conditions is less significant (Fig. 6e–g) and the SPD falls in between the 50 % and 100 % H (coverage during annealing) SPDs for $Pd_{75}Au_{25}$. This is because the surface segregation tendency of Cu in PdCu is much weaker than for Au in the case of PdAu, leading to a majority of Pd at the surface under all conditions (Fig. S12). Based on the H coverage contour lines in the vicinity of the operating region, $Pd_{75}Cu_{25}$ allows for slightly more H at the surface compared to Pd.

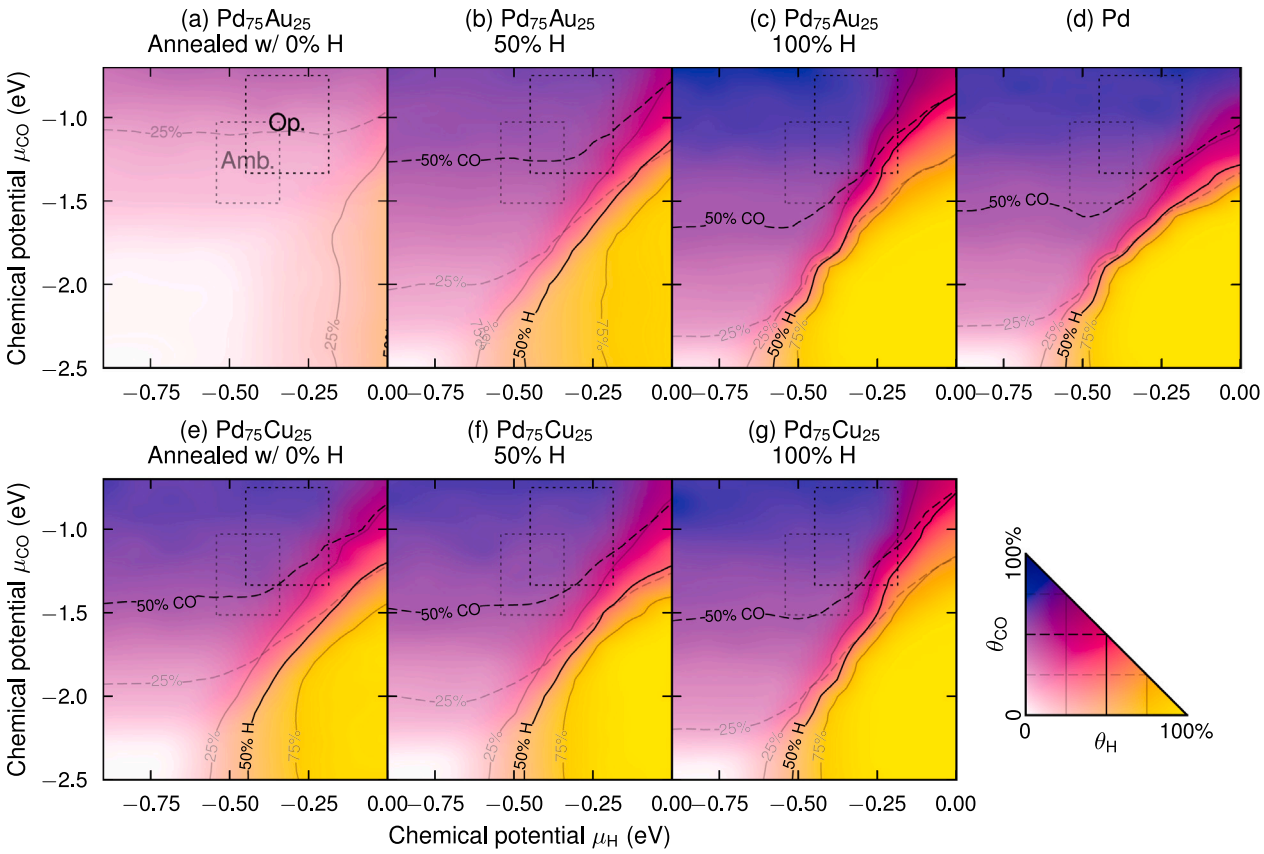

Fig. 6. SPD for Pd, $Pd_{75}Au_{25}$ and $Pd_{75}Cu_{25}$ {111} surfaces prepared in different conditions. The slab configurations were obtained from MC simulations at 773 K with (a) 0, (b) 50 or (c) 100 % H coverage and then covered with CO and H via MC simulations at 300 K while keeping the chemical configuration of the slab fixed. The surface coverage is represented by the color according to the colormap in the lower right corner and the contour lines, where the solid lines correspond to H and the dashed to CO. The dotted boxes indicate regions approximately corresponding to operating vs. ambient conditions. (For interpretation of the references to color in this figure legend, the reader is referred to the web version of this article.)

The indicated operating (and ambient) region spans a wide range of H and CO coverages, making it difficult to draw quantitative conclusions. We can, however, narrow this range by examining the SPDs in light of the experimental evidence. In particular, alloys with Cu (including the ternary alloys, see Fig. S19) are known to absorb a significant amount of H under operating conditions in the presence of CO [6,7]. This implies that (i) the samples were prepared with a high H coverage during annealing, and (ii) the lower right corner of the indicated region is most likely to represent the actual operating conditions. If either condition is not met, our results suggest that practically no H is adsorbed to the surface.

In summary, the coadsorption behavior of the alloys is governed primarily by the H coverage during annealing rather than the alloy composition. Fig. 7 shows that the H adsorption as a function of the H chemical potential shifts by at least 0.2 eV with the annealing H coverage, corresponding to several orders of magnitude in pressure (Fig. 5a–b). Surfaces annealed under H-poor conditions develop Au-rich surfaces that suppress adsorption of both species, while H-rich annealing yields Pd-rich surfaces that maintain significant H adsorption under operating conditions, outperforming pure Pd. Fig. 7 also indicates that the alloy composition plays a secondary role, as will be further discussed in the next section.

3.4. Influence of alloy composition

In the present work, we study binary (PdAu and PdCu) and ternary (PdAuCu) alloys, covering Au contents from 0% to 35% and Cu contents from 0% to 25%. Fig. 8 shows SPDs for $Pd_{75}Au_{25}$, $Pd_{65}Au_{35}$, and $Pd_{65}Au_{35}Cu_{10}$ prepared with 50 % H coverage (the upper right corner corresponds to Fig. 6b). As noted also in Fig. 7a, the CO and H coadsorption behavior is found to be independent of the alloy composition. In particular, there is no distinct effect of introducing Cu compared to Au, which is unexpected given the strong experimental evidence for Cu, specifically, reducing CO poisoning [6,7]. This (lack of a) trend remains across alloy compositions and preparation conditions (Fig. S19–S21), with the exception of the binary PdCu alloys, which show a different segregation behavior in the low-H preparation limit (see Fig. 6 as well as Fig. S12–S18).

Fig. 9 shows how the 50 % H adsorption contour line (from the SPDs) shifts with alloy composition, which can be interpreted as an indicator for the resistance to CO poisoning (with respect to adsorption thermodynamics). Three regions can be identified: the H adsorption limit at the bottom, the CO adsorption limit to the left, and the H–CO coadsorption limit in the upper right corner. In the H adsorption limit (lower right quadrant), Pd generally adsorbs more H than the alloys and the contour lines move to higher H chemical potentials with decreasing Pd content. A similar trend can be identified for CO, in the CO adsorption limit (upper left quadrant).

In the coadsorption limit (upper right quadrant), however, we see a shift in the trend where the 50 % H contour line for Pd crosses the corresponding contour lines for the alloys, meaning that the alloys adsorb more H at a given chemical potential. This suggests that in the coadsorption limit, alloying, in general, is beneficial for CO poisoning reduction. Depending on the preparation condition, this crossing of the contour lines happens inside (100 % H) or outside (0 % H) of the operating region ($\mu_H < -0.2$ eV). This suggests that a high H coverage during preparation is necessary to achieve the CO poisoning mitigating effects. We emphasize, however, again that there is a large uncertainty

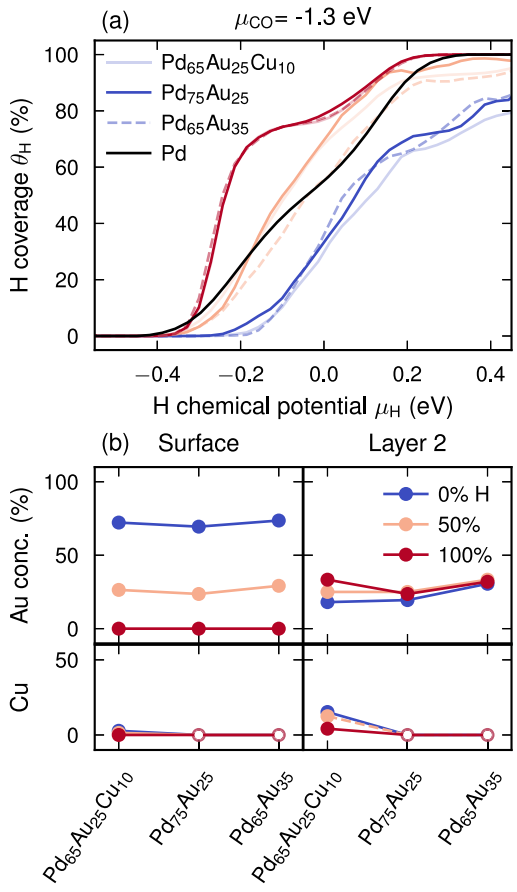

Fig. 7. H coverage and composition on Pd and PdAuCu-alloys. (a) H coverage as a function of the H chemical potential μ_H at fixed CO chemical potential μ_{CO} = −1.3 eV for Pd, $Pd_{65}Au_{25}Cu_{10}$, $Pd_{75}Au_{25}$ and $Pd_{65}Au_{35}$ obtained from MC simulations at 300 K and with the alloy configuration kept frozen. (b) Concentration of the surface layer and subsequent layer for the alloys, obtained from MC simulations at 773 K with varying H coverage as indicated by the legend (used also in a).

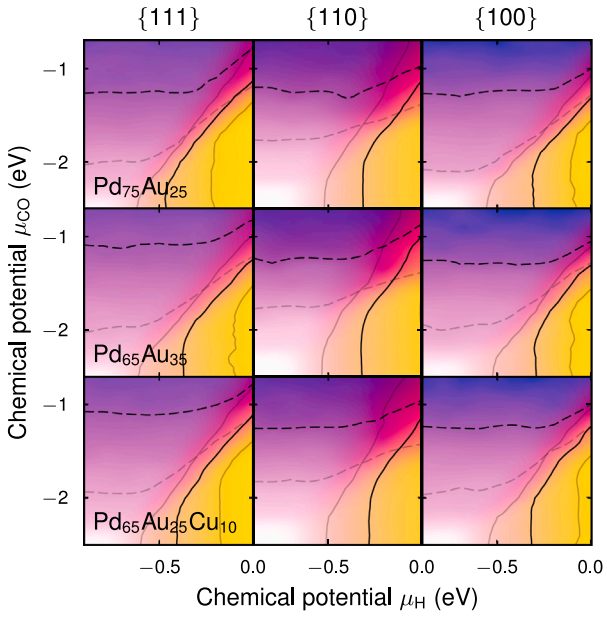

Fig. 8. Composition and orientation-dependent SPDs. SPD for $Pd_{75}Au_{25}$, $Pd_{65}Au_{35}$ and $Pd_{65}Au_{35}Cu_{10}$ at varying H and CO chemical potentials obtained from MC simulations at 300 K with alloy configuration kept frozen. The slab configurations are annealed at 773 K with 50 % H coverage. The coverages follow the same colormap as Fig. 6, with solid and dashed contour lines for H and CO, respectively. Note that for {110}, 100 % coverage corresponds to 2 ML of adsorbates due to the large surface area per metal atom. (For interpretation of the references to color in this figure legend, the reader is referred to the web version of this article.)

associated with the pressure conversion, and these predictions should be viewed as qualitative rather than quantitative.

For the systems prepared in 100 % H, the spread in the contour lines is generally narrow, which is reasonable since all systems have close to 100 % Pd at the surface (Fig. S12). In the coadsorption limit, however, all contour lines for the alloys distinctly deviate from the contour lines for Pd. This is surprising since their concentrations vary over a wide range *except* for the surface layer, which is nearly identical to the pure Pd case. It thus appears that any amount of alloyant in the bulk and subsurface region can distinctly change the adsorption behavior without entering the surface layer and without any dependence on the concentration.

In summary, we find no distinction between alloys with and without Cu in terms of CO poisoning resistance, despite the strong experimental evidence [6,7], based on *adsorption thermodynamics*. This holds across all studied compositions, preparation conditions, and partial pressures. We do, however, find that alloying in general increases the H-to-CO ratio in the coadsorption limit, which likely coincides with operating conditions for alloys prepared in a H-rich environment. Consistent with these findings, we hypothesize that under operating conditions, CO blocks the surface entirely for Pd and only partially for the alloys. To investigate the role of Cu specifically, we turn to the *kinetics* of H sorption into the bulk, specifically migration paths and associated kinetic barriers, via NEB calculations using the MACE model.

We consider {111} surfaces consisting of Pd with a single Au or Cu atom placed in atomic layer 1, 2, or 3, with a single H in the FCC adsorption site or one of the octahedral absorption sites, and map out all paths through the slab along with their associated kinetic barriers (Fig. 10). For PdAu, paths close to the Au atom are associated with a large increase in the energy of the initial and final states as well as the barrier. For PdCu, on the other hand, the migration energetics remain mostly unchanged or slightly improved compared to Pd. This suggests that the presence of Cu in the surface region could improve the *sorption kinetics*, especially in comparison to Au, and thereby enable H sorption in situations where the most favorable paths through the surface are blocked by CO.

At first glance, this negative impact of Au on H sorption appears to contradict prior studies, which demonstrate that Au enhances sorption kinetics in Pd-based alloys [5,78]. We argue, however, that while Au *globally* improves sorption kinetics, through lattice expansion [8,77] and a reduction in the total energy barrier for H sorption (mainly by increasing the adsorption energy) [78], it *locally* inhibits the kinetics for paths that pass an Au atom. This local effect becomes critical when the most energetically favorable H sorption paths are blocked by CO.

3.5. Influence of surface orientation

In the discussion above, we have mainly focused on the {111} surface, since it is the minimum energy surface for all three alloyants [79]. In the following we discuss the results for the additional {110} and {100} facets.

The adsorption energies on pure Pd are similar across the three surface orientations, with H and CO adsorbing at approximately −0.6 eV and −2.3 eV, respectively (Fig. 3b), and the increase in adsorption energy for Cu and Au is consistent across all facets (Fig. S4). The segregation energies for {111} and {100} are likewise very similar, with the expected tendency for Pd to segregate to the surface under H and CO,

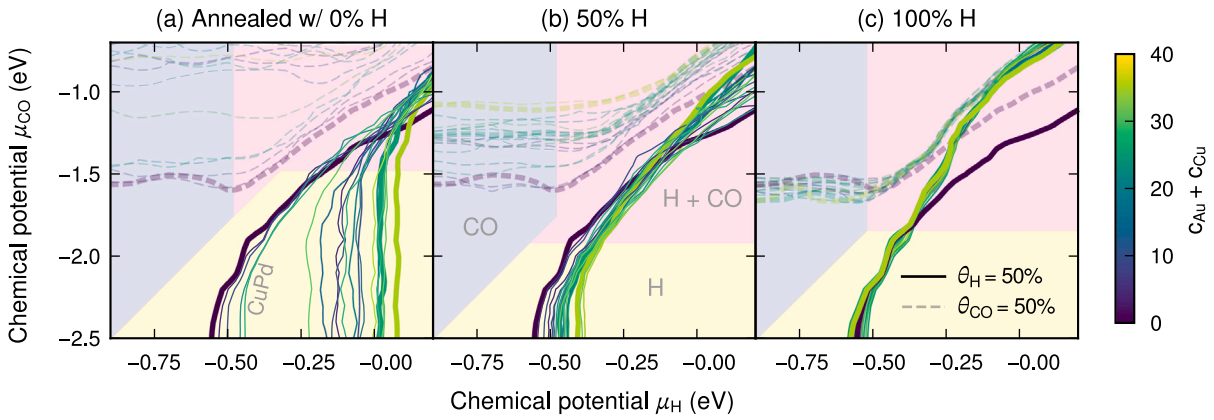

Fig. 9. 50% coverage contour lines for Pd and various PdAuCu alloy {111} surfaces. The slab configurations are obtained from MC simulations at 773 K with (a) 0 %, (b) 50 %, and (c) 100 % H coverage. The H and CO coverages are obtained from subsequent MC simulations at 300 K with fixed slab configuration. All alloy compositions considered are represented, with Pd, $Pd_{75}Au_{25}$, and $Pd_{65}Au_{25}Cu_{10}$ highlighted by thicker lines (see Fig. S12 for details concerning the compositions). The colored region indicates the limits of H, CO and H–CO adsorption. Note that the four studied PdCu alloys (see annotation in (a)) have a different segregation behavior than alloys with Au in the 0 % H coverage limit (a), affecting the behavior in the H and CO adsorption limits. (For interpretation of the references to color in this figure legend, the reader is referred to the web version of this article.)

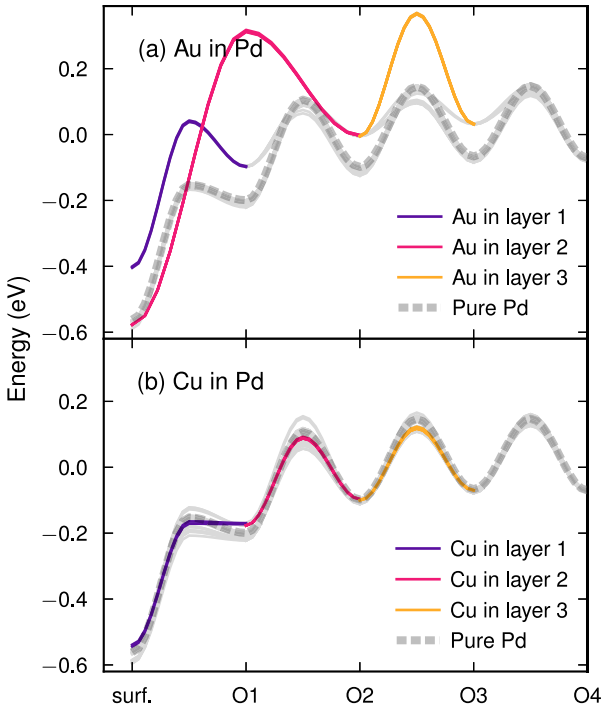

Fig. 10. Kinetic barriers for dilute Pd-alloys. Migration barriers for a H atom moving from the surface into the material via octahedral absorption sites, for pure Pd (dashed) and structures with a single (a) Au or (b) Cu atom placed in one of the three outermost atomic layers i.e., the surface region. The paths closest to the Au/Cu atom are highlighted by the colors indicated by the legend. Note that for the case of Au in layer 2, the O1 site is not stable and the H atom relaxes to the surface. (For interpretation of the references to color in this figure legend, the reader is referred to the web version of this article.)

for Au to segregate in vacuum, and a weak segregation tendency for Cu in PdCu alloys (Fig. 3a). The {110} surface is structurally distinct, with a row geometry that leaves the second atomic layer largely exposed (Fig. 2). While the segregation energies under CO are similar to the other facets, the driving force for segregation under H is much weaker on {110}. In vacuum, the preference for Au at the surface remains strong, and, in contrast to the other facets, there is a small preference for Cu at the surface in PdCu alloys (Fig. 3a).

The surface phase diagrams are overall very similar across all three surface orientations (Fig. 8), regardless of alloy composition or preparation condition (Fig. S19–S21). The main conclusion from the preceding sections therefore extends to all facets, namely that preparation conditions, rather than alloy composition or surface orientation, are the primary determinant of the coadsorption behavior.

Several minor orientation-dependent effects are, however, worth noting. The {100} surface behaves very similarly to {111}, consistent with the similar adsorption and segregation energetics. A slight tendency toward higher CO coverages is observed, with the CO contour lines shifted to lower μ_{CO} by a few tenths of an electronvolt relative to {111} (Fig. S22), which is associated with a slightly larger onset μ_H for H adsorption (Fig. S15). With regard to the Cu composition, however, we find a notable increase in H adsorption with Cu concentration in the lower right corner of the indicated operating conditions (Fig. S16). This is the only instance where Cu, specifically, shows a thermodynamic advantage for CO poisoning mitigation.

The {110} surface shows a noticeably reduced benefit of alloying compared to pure Pd in the coadsorption limit (Fig. S22). As a result, alloying is likely a less effective strategy for CO poisoning mitigation for this facet compared to the others. A further notable feature of {110} is the surprisingly strong H-induced segregation of Pd to the surface, in particular to the second atomic layer, given the modest Pd segregation energy (Fig. S13). In addition, Cu segregates strongly to the {110} surface in vacuum, in contrast to its weak segregation tendency on {111} and {100} surfaces (Fig. S13).

Still, we emphasize that overall, the coadsorption behavior is very similar across all three surface orientations, and the minor differences pointed out here are expected to have a limited impact on the experimentally observed behavior, given the strong preference for the {111} orientation in Pd-based nanoparticles [79].

Lastly, the present work does not take into account surface reconstruction, which is known to be induced by CO [80,81] and H [82] adsorption on Pd{110}, as well as by H sorption into the bulk on all low-index Pd surfaces [83]. While reconstruction could in principle be incorporated in a CE framework, it constitutes a substantial extension. This limitation is consistent with the aim of this work, namely the initial adsorption process on pristine surfaces, which also does not consider H sorption into the bulk, surface defects, or the complexity of real, polycrystalline nanoparticles. Reconstruction effects could, however, potentially alter the coadsorption behavior, in particular for the {110} surface, and represent a possible direction for future work.

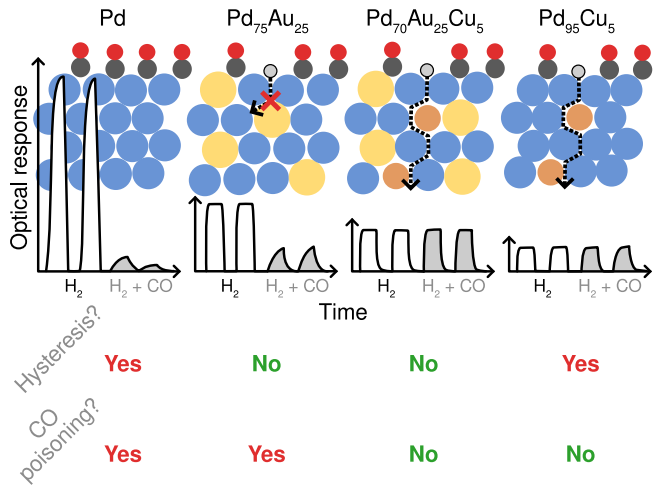

Fig. 11. Proposed mechanism for Cu-induced CO poisoning resistance. The upper panel shows the (absolute) shift in optical response of Pd, $Pd_{75}Au_{25}$, $Pd_{70}Au_{25}Cu_5$, and $Pd_{95}Cu_5$ when subjected to pulses of H_2 (40 mbar) vs. H_2 (40 mbar) + CO (5 mbar), adapted from [6]. Here, Pd and the PdAu alloy show clear signs of CO poisoning, with a more moderate effect for the alloy, while alloys with Cu are unaffected by CO. The slab representations show the corresponding proposed slab–CO–H interplay, where CO fully blocks H sorption in Pd but only partially for the alloys and near-surface Au locally inhibits H absorption, while Cu preserves viable absorption pathways. The lower panel summarizes the experimentally observed CO poisoning [6,7] and hysteresis (Fig. S1) characteristics.

4. Conclusions

In the present work, we have studied the coadsorption of H and CO on PdAuCu alloy surfaces with 0 % to 35 % Au and 0 % to 25 % Cu to understand the mitigating effect on CO poisoning of such alloys, compared to Pd, in the context of H_2 sensing. Experimentally, alloying with Cu has been found to completely eliminate CO poisoning in Pd-based alloys [6,7]. Alloying with Au, which is crucial for hysteresis reduction, does not have the same benefit, although the CO poisoning is reduced compared to pure Pd (Fig. 11).

We find that the coadsorption behavior under operation is governed by the H coverage during annealing rather than the alloy composition. Au-rich surfaces, formed under H-poor preparation conditions, suppress both CO and H adsorption, while H-rich preparation yields Pd-rich surfaces that promote adsorption of both species. In the coadsorption limit, Pd-rich alloy surfaces maintain a higher H-to-CO ratio compared to pure Pd, suggesting improved CO poisoning resistance. Mapping the coadsorption limit to CO and H_2 partial pressures is difficult due to the large uncertainty associated with the chemical potential to partial pressure conversion, but we find the overlap with operating conditions likely. Strikingly, this improvement is insensitive to alloy composition. The coadsorption behavior of PdAuCu alloys is indistinguishable from that of PdAu across all studied compositions, orientations, and preparation conditions, which rules out *adsorption thermodynamics* as the origin of the experimentally observed Cu-specific CO poisoning mitigation.

The experimentally observed optical shifts in response to H_2 vs. a mixture of H_2 and CO (Fig. 11) reveal that the primary difference between the samples during CO exposure is not the absolute H sorption, but rather the relative H sorption compared to the CO-free case and, importantly, the *sorption kinetics*. With regard to the kinetics, we find that in the dilute alloy limit, absorption paths via Au atoms are highly unfavorable, while swapping a Pd atom for Cu leaves the absorption kinetics unchanged compared to pure Pd.

By combining these findings with the experimental evidence that Cu completely mitigates CO poisoning while Au has a much smaller positive effect, we propose the following hypothesis. Alloying in general leads to an increased H-to-CO ratio, and Cu is necessary to preserve viable H absorption pathways when CO blocks the most favorable Pd-dominated paths. Further studies of the bulk absorption process under realistic CO coverage conditions are necessary to confirm this proposed mechanism. The MLIPs developed in the present work for the PdAuCu:(H,CO) system provide an ideal starting point for this endeavor.

CRediT authorship contribution statement

Pernilla Ekborg-Tanner: Writing – review & editing, Writing – original draft, Visualization, Validation, Project administration, Methodology, Investigation, Formal analysis, Data curation, Conceptualization. **Paul Erhart:** Writing – review & editing, Supervision, Project administration, Methodology, Funding acquisition, Data curation, Conceptualization.

Declaration of competing interest

The authors declare the following financial interests/personal relationships which may be considered as potential competing interests: Paul Erhart reports financial support was provided by Chalmers University of Technology. Paul Erhart reports financial support was provided by Swedish Research Council. If there are other authors, they declare that they have no known competing financial interests or personal relationships that could have appeared to influence the work reported in this paper.

Acknowledgments

We gratefully acknowledge funding from the Swedish Research Council (Nos. 2020-04935 and 2021-05072) and the Area of Advance at Nano at Chalmers as well as computational resources provided by the National Academic Infrastructure for Supercomputing in Sweden at NSC, PDC, and C3SE partially funded by the Swedish Research Council through grant agreement No. 2022-06725, as well as the Berzelius resource provided by the Knut and Alice Wallenberg Foundation at NSC.

Appendix A. Supplementary data

Supplementary material related to this article can be found online at https://doi.org/10.1016/j.actamat.2026.122507.

Data availability

The NEP and MACE models as well as the database of DFT calculations used to train these models have been deposited in the Zenodo database under accession code https://doi.org/10.5281/zenodo.17670908.

References

[1] O.M. Løvvik, S.M. Opalka, Reversed surface segregation in palladium-silver alloys due to hydrogen adsorption, Surf. Sci. 602 (17) (2008) 2840–2844, http://dx.doi.org/10.1016/j.susc.2008.07.016.

[2] P. Ekborg-Tanner, P. Erhart, Hydrogen-driven surface segregation in Pd alloys from atomic-scale simulations, J. Phys. Chem. C 125 (31) (2021) 17248–17260, http://dx.doi.org/10.1021/acs.jpcc.1c00575.

[3] C. Langhammer, E.M. Larsson, B. Kasemo, I. Zorić, Indirect nanoplasmonic sensing: Ultrasensitive experimental platform for nanomaterials science and optical nanocalorimetry, Nano Lett. 10 (9) (2010) 3529–3538, http://dx.doi.org/10.1021/nl101727b.

[4] J. Wellendorff, T.L. Silbaugh, D. Garcia-Pintos, J.K. Nørskov, T. Bligaard, F. Studt, C.T. Campbell, A benchmark database for adsorption bond energies to transition metal surfaces and comparison to selected DFT functionals, Surf. Sci. 640 (2015) 36–44, http://dx.doi.org/10.1016/j.susc.2015.03.023.

[5] C. Wadell, F.A.A. Nugroho, E. Lidström, B. Iandolo, J.B. Wagner, C. Langhammer, Hysteresis-free nanoplasmonic Pd-Au alloy hydrogen sensors, Nano Lett. 15 (5) (2015) 3563–3570, http://dx.doi.org/10.1021/acs.nanolett.5b01053.

[6] I. Darmadi, F.A.A. Nugroho, S. Kadkhodazadeh, J.B. Wagner, C. Langhammer, Rationally designed pdaucu ternary alloy nanoparticles for intrinsically deactivation-resistant ultrafast plasmonic hydrogen sensing, ACS Sens. 4 (5) (2019) 1424–1432, http://dx.doi.org/10.1021/acssensors.9b00610.

[7] I. Darmadi, S.Z. Khairunnisa, D. Tomeček, C. Langhammer, Optimization of the composition of pdaucu ternary alloy nanoparticles for plasmonic hydrogen sensing, ACS Appl. Nano Mater. 4 (2021) 8716, http://dx.doi.org/10.1021/acsanm.1c01242.

[8] J.M. Rahm, J. Löfgren, E. Fransson, P. Erhart, A tale of two phase diagrams: Interplay of ordering and hydrogen uptake in Pd–Au–H, Acta Mater. 211 (2021) 116893, http://dx.doi.org/10.1016/j.actamat.2021.116893.

[9] A. Bajpai, K. Frey, W.F. Schneider, Binary approach to ternary cluster expansions: NO–O–vacancy system on Pt(111), J. Phys. Chem. C 121 (13) (2017) 7344–7354, http://dx.doi.org/10.1021/acs.jpcc.7b00914.

[10] A.J. Samin, C.D. Taylor, A combined density functional theory and Monte Carlo investigation of the competitive adsorption of atomic oxygen and chlorine to the Ni (111) surface, J. Electrochem. Soc. 165 (7) (2018) C302, http://dx.doi.org/10.1149/2.0031807jes.

[11] A.J.R. Hensley, G. Collinge, Y. Wang, J.-S. McEwen, Coverage-dependent adsorption of hydrogen on Fe(100): Determining catalytically relevant surface structures via lattice gas models, J. Phys. Chem. C 124 (13) (2020) 7254–7266, http://dx.doi.org/10.1021/acs.jpcc.9b11945.

[12] S. Müller, M. Stöhr, O. Wieckhorst, Structure and stability of binary alloy surfaces: Segregation, relaxation, and ordering from first-principles calculations, Appl. Phys. A 82 (3) (2006) 415–419, http://dx.doi.org/10.1007/s00339-005-3362-6.

[13] W. Chen, P. Dalach, W.F. Schneider, C. Wolverton, Interplay between subsurface ordering, surface segregation, and adsorption on Pt–Ti(111) near-surface alloys, Langmuir 28 (10) (2012) 4683–4693, http://dx.doi.org/10.1021/la204843q.

[14] E. Christoffersen, P. Stoltze, J.K. Nørskov, Monte Carlo simulations of adsorption-induced segregation, Surf. Sci. 505 (2002) 200–214, http://dx.doi.org/10.1016/S0039-6028(02)01158-5.

[15] K. Andersson, F. Calle-Vallejo, J. Rossmeisl, I. Chorkendorff, Adsorption-driven surface segregation of the less reactive alloy component, J. Am. Chem. Soc. 131 (6) (2009) 2404–2407, http://dx.doi.org/10.1021/ja8089087.

[16] H.Y. Kim, G. Henkelman, CO adsorption-driven surface segregation of Pd on Au/Pd bimetallic surfaces: Role of defects and effect on CO oxidation, ACS Catal. 3 (2013) 2541–2546, http://dx.doi.org/10.1021/CS4006259.

[17] P. West, R. Johnston, G. Barcaro, A. Fortunelli, Effect of CO and H adsorption on the compositional structure of binary nanoalloys via DFT modeling, Eur. Phys. J. D 67 (2013) 1–9, http://dx.doi.org/10.1140/EPJD/E2013-40257-4.

[18] B. Han, A. Van Der Ven, G. Ceder, B. Hwang, Surface segregation and ordering of alloy surfaces in the presence of adsorbates, Phys. Rev. B 72 (2005) 205409, http://dx.doi.org/10.1103/PHYSREVB.72.205409.

[19] C. Li, D. Raciti, T. Pu, L. Cao, C. He, C. Wang, T. Mueller, Improved prediction of nanoalloy structures by the explicit inclusion of adsorbates in cluster expansions, J. Phys. Chem. C (2018) http://dx.doi.org/10.1021/ACS.JPCC.8B03868.

[20] Q. Ye, Y. Cheng, L. Cao, Surface segregation-driven composition–activity mapping of high-entropy alloy nanoparticles for oxygen reduction reaction, ACS Catal. 16 (3) (2026) 2149–2159, http://dx.doi.org/10.1021/acscatal.5c06492.

[21] A.R. Natarajan Y.L. Müller, Constructing multicomponent cluster expansions with machine-learning and chemical embedding, Npj Comput. Mater. 11 (1) (2025) 60, http://dx.doi.org/10.1038/s41524-025-01543-3.

[22] M.R.K. Musa, Y. Qian, J. Peng, D. Cereceda, Accelerating the discovery of low-energy structure configurations: A computational approach that integrates first-principles calculations, Monte Carlo sampling, and machine learning, 2024, http://dx.doi.org/10.1016/j.scriptamat.2024.116535, ArXiv abs/2410.05604.

[23] J.R. Boes, J.R. Kitchin, Modeling segregation on Aupd(111) surfaces with density functional theory and Monte Carlo simulations, J. Phys. Chem. C 121 (6) (2017) 3479–3487, http://dx.doi.org/10.1021/acs.jpcc.6b12752.

[24] M. Liu, Y. Yang, J.R. Kitchin, Semi-grand canonical Monte Carlo simulation of the acrolein induced surface segregation and aggregation of Agpd with machine learning surrogate models, J. Chem. Phys. 154 (13) (2021) 134701, http://dx.doi.org/10.1063/5.0046440.

[25] Y. Yang, Z. Guo, A.J. Gellman, J.R. Kitchin, Simulating segregation in a ternary Cu–Pd–Au alloy with density functional theory, machine learning, and Monte Carlo simulations, J. Phys. Chem. C 126 (4) (2022) 1800–1808, http://dx.doi.org/10.1021/acs.jpcc.1c09647.

[26] K. Broderick, R.A. Burnley, A.J. Gellman, J.R. Kitchin, Surface segregation studies in ternary noble metal alloys: Comparing DFT and machine learning with experimental data, ChemPhysChem 25 (13) (2024) e202400073, http://dx.doi.org/10.1002/cphc.202400073.

[27] A. Mazitov, M.A. Springer, N. Lopanitsyna, G. Fraux, S. De, M. Ceriotti, Surface segregation in high-entropy alloys from alchemical machine learning, 7, (2) 2024, 025007, http://dx.doi.org/10.1088/2515-7639/ad2983,

[28] J.M. Sanchez, F. Ducastelle, D. Gratias, Generalized cluster description of multicomponent systems, Physica 128 (1–2) (1984) 334.

[29] D.C. Beaudry, M.J. Waters, G.M. Valentino, D.L. Foley, E. Anber, Y. Rakita, C.J. Brandenburg, J.-P. Couzinié, L. Perrière, T. Aoki, K.E. Knipling, P.G. Callahan, B.W. Redemann, T.M. McQueen, E.J. Opila, J.M. Rondinelli, M.L. Taheri, Exceptional hardness in multiprincipal element alloys via hierarchical oxygen heterogeneities, Sci. Adv. 10 (38) (2024) eado9697, http://dx.doi.org/10.1126/sciadv.ado9697.

[30] T. Mueller, G. Ceder, Bayesian approach to cluster expansions, Phys. Rev. B 80 (2) (2009) 024103, http://dx.doi.org/10.1103/PhysRevB.80.024103.

[31] J. Zhang, X. Liu, S. Bi, J. Yin, G. Zhang, M. Eisenbach, Robust data-driven approach for predicting the configurational energy of high entropy alloys, Mater. Des. 185 (2020) 108247, http://dx.doi.org/10.1016/j.matdes.2019.108247.

[32] M.F. Shojaei, J. Holber, S. Das, G.H. Teichert, T. Mueller, L. Hung, V. Gavini, K. Garikipati, Bridging scales with machine learning: From first principles statistical mechanics to continuum phase field computations to study order–disorder transitions in Li_xCoO_2, J. Mech. Phys. Solids 190 (2024) 105726, http://dx.doi.org/10.1016/j.jmps.2024.105726.

[33] B. Sadigh, P. Erhart, A. Stukowski, A. Caro, E. Martinez, L. Zepeda-Ruiz, Scalable parallel Monte Carlo algorithm for atomistic simulations of precipitation in alloys, Phys. Rev. B 85 (18) (2012) 184203, http://dx.doi.org/10.1103/PhysRevB.85.184203.

[34] K. Song, R. Zhao, J. Liu, Y. Wang, E. Lindgren, Y. Wang, S. Chen, K. Xu, T. Liang, P. Ying, N. Xu, Z. Zhao, J. Shi, J. Wang, S. Lyu, Z. Zeng, S. Liang, H. Dong, L. Sun, Y. Chen, Z. Zhang, W. Guo, P. Qian, J. Sun, P. Erhart, T. Ala-Nissila, Y. Su, Z. Fan, General-purpose machine-learned potential for 16 elemental metals and their alloys, Nat. Commun. 15 (2024) 10208, http://dx.doi.org/10.1038/s41467-024-54554-x.

[35] Z. Fan, Y. Wang, P. Ying, K. Song, J. Wang, Y. Wang, Z. Zeng, K. Xu, E. Lindgren, J.M. Rahm, A.J. Gabourie, J. Liu, H. Dong, J. Wu, Y. Chen, Z. Zhong, J. Sun, P. Erhart, Y. Su, T. Ala-Nissila, Gpumd: A package for constructing accurate machine-learned potentials and performing highly efficient atomistic simulations, J. Chem. Phys. 157 (2022) 114801, http://dx.doi.org/10.1063/5.0106617.

[36] D. Wierstra, T. Schaul, T. Glasmachers, Y. Sun, J. Peters, J. Schmidhuber, Natural evolution strategies, J. Mach. Learn. Res. 15 (27) (2014) 949–980.

[37] E. Fransson, J. Wiktor, P. Erhart, Phase transitions in inorganic halide perovskites from machine-learned potentials, J. Phys. Chem. C 127 (2023) 13773, http://dx.doi.org/10.1021/acs.jpcc.3c01542.

[38] K. Xu, H. Bu, S. Pan, E. Lindgren, Y. Wu, Y. Wang, J. Liu, K. Song, B. Xu, Y. Li, T. Hainer, L. Svensson, J. Wiktor, R. Zhao, H. Huang, C. Qian, S. Zhang, Z. Zeng, B. Zhang, B. Tang, Y. Xiao, Z. Yan, J. Shi, Z. Liang, J. Wang, T. Liang, S. Cao, Y. Wang, P. Ying, N. Xu, C. Chen, Y. Zhang, Z. Chen, X. Wu, W. Jiang, E. Berger, Y. Li, S. Chen, A.J. Gabourie, H. Dong, S. Xiong, N. Wei, Y. Chen, J. Xu, F. Ding, Z. Sun, T. Ala-Nissila, A. Harju, J. Zheng, P. Guan, P. Erhart, J. Sun, W. Ouyang, Y. Su, Z. Fan, Gpumd 4.0: A high-performance molecular dynamics package for versatile materials simulations with machine-learned potentials, Mater. Genome Eng. Adv. 3 (2025) e70028, http://dx.doi.org/10.1002/mgea.70028.

[39] E. Lindgren, J.M. Rahm, E. Fransson, F. Eriksson, N. Österbacka, Z. Fan, P. Erhart, Calorine: A python package for constructing and sampling neuroevolution potential models, J. Open Source Softw. 9 (2024) 6264, http://dx.doi.org/10.21105/joss.06264.

[40] G.L.W. Hart, R.W. Forcade, Algorithm for generating derivative structures, Phys. Rev. B 77 (2008) 224115, http://dx.doi.org/10.1103/PhysRevB.77.224115.

[41] G.L. Hart, R.W. Forcade, Generating derivative structures from multilattices: Algorithm and application to hcp alloys, Phys. Rev. B 80 (1) (2009) 014120, http://dx.doi.org/10.1103/PhysRevB.80.014120.

[42] G. Henkelman, H. Jonsson, Improved tangent estimate in the neb method for finding minimum energy paths and saddle points, J. Chem. Phys. 113 (2000) 9978–9985, http://dx.doi.org/10.1063/1.1323224.

[43] G. Henkelman, B.P. Uberuaga, H. Jonsson, A climbing-image neb method for finding saddle points and minimum energy paths, J. Chem. Phys. 113 (2000) 9901–9904, http://dx.doi.org/10.1063/1.1329672.

[44] P. Lindgren, G. Kastlunger, A.A. Peterson, Scaled and dynamic optimizations of nudged elastic bands, J. Chem. Theory Comput. 15 (11) (2019) 5787–5793, http://dx.doi.org/10.1021/acs.jctc.9b00633.

[45] A.H. Larsen, J.J. Mortensen, J. Blomqvist, I.E. Castelli, R. Christensen, M. Dułak, J. Friis, M.N. Groves, B. Hammer, C. Hargus, E.D. Hermes, P.C. Jennings, P. Bjerre Jensen, J. Kermode, J.R. Kitchin, E. Leonhard Kolsbjerg, J. Kubal, K. Kaasbjerg, S. Lysgaard, J. Bergmann Maronsson, T. Maxson, T. Olsen, L. Pastewka, A. Peterson, C. Rostgaard, J. Schiøtz, O. Schütt, M. Strange, K.S. Thygesen, T. Vegge, L. Vilhelmsen, M. Walter, Z. Zeng, K.W. Jacobsen, The atomic simulation environment—a python library for working with atoms, J. Phys.: Condens. Matter. 29 (27) (2017) 273002, http://dx.doi.org/10.1088/1361-648X/aa680e.

[46] F. Eriksson, E. Fransson, P. Erhart, The hiphive package for the extraction of high-order force constants by machine learning, Adv. Theory Simul. 2 (2019) 1800184, http://dx.doi.org/10.1002/adts.201800184.

[47] M. Ångqvist, W.A. Muñoz, J.M. Rahm, E. Fransson, C. Durniak, P. Rozyczko, T.H. Rod, P. Erhart, ICET – a python library for constructing and sampling alloy cluster expansions, Adv. Theory Simul. (2) (2019) 1900015, http://dx.doi.org/10.1002/adts.201900015.

[48] P. Ekborg-Tanner, P. Rosander, E. Fransson, P. Erhart, Construction and sampling of alloy cluster expansions—A tutorial, PRX Energy 3 (4) (2024) 042001, http://dx.doi.org/10.1103/PRXEnergy.3.042001.
[49] I. Batatia, D.P. Kovacs, G.N.C. Simm, C. Ortner, G. Csanyi, MACE: Higher order equivariant message passing neural networks for fast and accurate force fields, in: A.H. Oh, A. Agarwal, D. Belgrave, K. Cho (Eds.), Advances in Neural Information Processing Systems, Curran Associates, Inc., 2022, http://dx.doi.org/10.48550/arXiv.2206.07697, arXiv:2206.07697.
[50] I. Batatia, S. Batzner, D.P. Kovács, A. Musaelian, G.N.C. Simm, R. Drautz, C. Ortner, B. Kozinsky, G. Csányi, The design space of e(3)-equivariant atom-centered interatomic potentials, 2022, http://dx.doi.org/10.48550/arXiv.2205.06643, arXiv:2205.06643.
[51] M. Dion, H. Rydberg, E. Schröder, D.C. Langreth, B.I. Lundqvist, Van der waals density functional for general geometries, Phys. Rev. Lett. 92 (2004) 246401, http://dx.doi.org/10.1103/PhysRevLett.92.246401.
[52] K. Berland, P. Hyldgaard, Exchange functional that tests the robustness of the plasmon description of the van der Waals density functional, Phys. Rev. B 89 (2014) 035412, http://dx.doi.org/10.1103/PhysRevB.89.035412.
[53] G. Kresse, J. Furthmüller, Efficiency of ab-initio total energy calculations for metals and semiconductors using a plane-wave basis set, Comput. Mater. Sci. 6 (1) (1996) 15–50, http://dx.doi.org/10.1016/0927-0256(96)00008-0.
[54] G. Kresse, J. Furthmüller, Efficient iterative schemes for ab initio total-energy calculations using a plane-wave basis set, Phys. Rev. B 54 (16) (1996) 11169–11186, http://dx.doi.org/10.1103/PhysRevB.54.11169.
[55] P.E. Blöchl, Projector augmented-wave method, Phys. Rev. B 50 (24) (1994) 17953–17979, http://dx.doi.org/10.1103/PhysRevB.50.17953.
[56] G. Kresse, D. Joubert, From ultrasoft pseudopotentials to the projector augmented-wave method, Phys. Rev. B 59 (3) (1999) 1758–1775, http://dx.doi.org/10.1103/PhysRevB.59.1758.
[57] R. Tibshirani, Regression shrinkage and selection via the Lasso, J. R. Stat. Soc. Ser. B Stat. Methodol. 58 (1) (1996) 267–288, http://dx.doi.org/10.1111/j.2517-6161.1996.tb02080.x.
[58] D.J.C. MacKay, Bayesian non-linear modelling for the prediction competition, ASHRAE Trans. (1994) 1053–1062, V.100, Pt.2.
[59] F. Pedregosa, G. Varoquaux, A. Gramfort, V. Michel, B. Thirion, O. Grisel, M. Blondel, P. Prettenhofer, R. Weiss, V. Dubourg, J. Vanderplas, A. Passos, D. Cournapeau, M. Brucher, M. Perrot, E. Duchesnay, Scikit-learn: Machine learning in python, J. Mach. Learn. Res. 12 (2011) 2825–2830.
[60] E. Fransson, F. Eriksson, P. Erhart, Efficient construction of linear models in materials modeling and applications to force constant expansions, Npj Comput. Mater. 6 (2020) http://dx.doi.org/10.1038/s41524-020-00404-5.
[61] L. Li, X. Li, Z. Duan, R.J. Meyer, R. Carr, S. Raman, L. Koziol, G. Henkelman, Adaptive kinetic Monte Carlo simulations of surface segregation in Pdau nanoparticles, Nanoscale 11 (21) (2019) 10524–10535, http://dx.doi.org/10.1039/C9NR01858A.
[62] J.M. Polfus, T. Peters, R. Bredesen, O.M. Løvvik, Vacancy diffusion in palladium hydrides, Phys. Chem. Chem. Phys. 23 (24) (2021) 13680–13686, http://dx.doi.org/10.1039/D1CP01960K.
[63] T. Mitsui, M.K. Rose, E. Fomin, D.F. Ogletree, M. Salmeron, Dissociative hydrogen adsorption on palladium requires aggregates of three or more vacancies, Nature 422 (6933) (2003) 705–707, http://dx.doi.org/10.1038/nature01557.
[64] T. Engel, H. Kuipers, A molecular-beam investigation of the scattering, adsorption and absorption of H_2 and D_2 from/on/in Pd(111), Surf. Sci. 90 (1) (1979) 162–180, http://dx.doi.org/10.1016/0039-6028(79)90017-7.
[65] M. Wilde, M. Matsumoto, K. Fukutani, T. Aruga, Depth-resolved analysis of subsurface hydrogen absorbed by Pd(100), Surf. Sci. 482–485 (2001) 346–352, http://dx.doi.org/10.1016/S0039-6028(01)00727-0.
[66] M.W. Chase, N.I. of Standards, Technology, NIST-JANAF Thermochemical Tables, fourth ed., NIST Standard Reference Database Number 13, 1998, http://dx.doi.org/10.18434/T42S31, https://janaf.nist.gov/.
[67] H. Unterhalt, G. Rupprechter, H.-J. Freund, Vibrational sum frequency spectroscopy on Pd(111) and supported Pd nanoparticles: CO adsorption from ultrahigh vacuum to atmospheric pressure, J. Phys. Chem. B 106 (2) (2002) 356–367, http://dx.doi.org/10.1021/jp013000+.
[68] W.K. Kuhn, J. Szanyi, D.W. Goodman, CO adsorption on Pd(111): the effects of temperature and pressure, Surf. Sci. 274 (3) (1992) L611–L618, http://dx.doi.org/10.1016/0039-6028(92)90834-S.
[69] V.V. Kaichev, I.P. Prosvirin, V.I. Bukhtiyarov, H. Unterhalt, G. Rupprechter, H.-J. Freund, High-pressure studies of CO adsorption on Pd(111) by X-ray photoelectron spectroscopy and sum-frequency generation, J. Phys. Chem. B 107 (15) (2003) 3522–3527, http://dx.doi.org/10.1021/jp021992t.
[70] J.W. He, U. Memmert, K. Griffiths, W.N. Lennard, P.R. Norton, Absolute coverages for the various surface phases of CO and o adsorbed on Pd(110), Surf. Sci. 202 (3) (1988) L555–L558, http://dx.doi.org/10.1016/0039-6028(88)90031-3.
[71] J. He, P.R. Norton, Interaction of CO with a Pd(110) surface, studied by low energy electron diffraction, thermal desorption spectroscopy, and $\Delta\Phi$, J. Chem. Phys. 89 (2) (1988) 1170–1176, http://dx.doi.org/10.1063/1.455225.
[72] R.J. Behm, K. Christmann, G. Ertl, M.A. Van Hove, Adsorption of Co on Pd(100), J. Chem. Phys. 73 (6) (1980) 2984–2995, http://dx.doi.org/10.1063/1.440430.
[73] O.M. Løvvik, R.A. Olsen, Adsorption energies and ordered structures of hydrogen on Pd(111) from density-functional periodic calculations, Phys. Rev. B 58 (16) (1998) 10890–10898, http://dx.doi.org/10.1103/PhysRevB.58.10890.
[74] J. Szanyi, W.K. Kuhn, D.W. Goodman, CO adsorption on Pd(111) and Pd(100): Low and high pressure correlations, J. Vac. Sci. Technol. A 11 (4) (1993) 1969–1974, http://dx.doi.org/10.1116/1.578532.
[75] N.N.W. Service, Jetstream: An online school for weather, 2025, https://www.noaa.gov/jetstream/atmosphere. (Accessed 15 February 2025).
[76] U.S. Department of Energy, Energy efficiency and renewable energy (EERE), in: Fuel Cell Technologies Office, Multi-Year Research, Development, and Demonstration Plan, 2011–2020: Section 3.7 Hydrogen Safety, Codes and Standards, 2015.
[77] I. Darmadi, F.A.A. Nugroho, C. Langhammer, High-performance nanostructured palladium-based hydrogen sensors-current limitations and strategies for their mitigation, ACS Sensors 5 (11) (2020) 3306–3327, http://dx.doi.org/10.1021/acssensors.0c02019.
[78] K. Namba, S. Ogura, S. Ohno, W. Di, K. Kato, M. Wilde, I. Pletikosić, P. Pervan, M. Milun, K. Fukutani, Acceleration of hydrogen absorption by palladium through surface alloying with gold, Proc. Natl. Acad. Sci. 115 (31) (2018) 7896–7900, http://dx.doi.org/10.1073/pnas.1800412115.
[79] R. Tran, Z. Xu, B. Radhakrishnan, D. Winston, W. Sun, K.A. Persson, S.P. Ong, Surface energies of elemental crystals, Sci. Data 3 (1) (2016) http://dx.doi.org/10.1038/sdata.2016.80.
[80] P. Hu, L. De La Garza, R. Raval, D. King, A LEED structural study of the CO induced reconstruction of Pd{110} evidence for a missing row structure, Surf. Sci. 249 (1–3) (1991) 1–7, http://dx.doi.org/10.1016/0039-6028(91)90827-F.
[81] M. Ramsey, F. Leisenberger, F. Netzer, A. Roberts, R. Raval, High-resolution core-level photoemission of the CO-induced Pd(110) surface reconstruction, Surf. Sci. 385 (1) (1997) 207–215, http://dx.doi.org/10.1016/S0039-6028(97)00282-3.
[82] H. Niehus, C. Hiller, G. Comsa, Row pairing induced by hydrogen adsorption at Pd(110), Surf. Sci. 173 (2) (1986) L599–L605, http://dx.doi.org/10.1016/0039-6028(86)90185-8.
[83] A. Ngoipala, C. Schott, V. Briega-Martos, M. Qamar, M. Mrovec, S. Javan Nikkhah, T.O. Schmidt, L. Deville, A. Capogrosso, L. Moumaneix, T. Kallio, A. Viola, F. Maillard, R. Drautz, A.S. Bandarenka, S. Cherevko, M. Vandichel, E.L. Gubanova, Hydride-induced reconstruction of Pd electrode surfaces: A combined computational and experimental study, Adv. Mater. 37 (4) (2025) 2410951, http://dx.doi.org/10.1002/adma.202410951.